

Fe, Cu-Coordinated ZIF-Derived Carbon Framework for Efficient Oxygen Reduction Reaction and Zinc–Air Batteries

Zhihao Wang, Huihui Jin, Tian Meng, Ke Liao, Wenqian Meng, Jinlong Yang, Daping He,* Yuli Xiong,* and Shichun Mu*

Zeolitic imidazole frameworks (ZIFs) offer rich platforms for rational design and construction of high-performance nonprecious-metal oxygen reduction reaction (ORR) catalysts owing to their flexibility, hierarchical porous structures, and high surface area. Herein, an Fe, Cu-coordinated ZIF-derived carbon framework (Cu@Fe-N-C) with a well-defined morphology of truncated rhombic dodecahedron is facilely prepared by introducing Fe²⁺ and Cu²⁺ during the growth of ZIF-8, followed by pyrolysis. The obtained Cu@Fe-N-C, with bimetallic active sites, large surface area, high nitrogen doping level, and conductive carbon frameworks, exhibits excellent ORR performance. It displays 50 mV higher half-wave potential (0.892 V) than that of Pt catalysts in an alkaline medium and comparable performance to Pt catalysts in an acidic medium. In addition, it also has excellent durability and methanol resistance ability in both acidic and alkaline solutions, which makes it one of the best Pt-free catalysts reported to date for ORR. Impressively, when being employed as a cathode catalyst in zinc–air batteries, Cu@Fe-N-C presents a higher peak power density of 92 mW cm⁻² than that of Pt/C (74 mW cm⁻²) as well as excellent durability.

1. Introduction


Oxygen reduction reaction (ORR) plays a very important role in electrochemical energy conversion and storage systems (such as fuel cell and metal–air battery, etc.).^[1] However, the hysteresis of cathode ORR rate seriously restricts the development of oxygen reduction electrochemical devices. At present, the platinum (Pt)-based metals are the state-of-the-art electrocatalysts due to their low overpotentials.^[2] However, the high cost, limited reserve, poor durability, and chemical susceptibility significantly restrict their large-scale commercial

applications.^[3] Thus, great efforts have been made to obtain high-performance Pt-free electrocatalysts such as Pt-free alloys, metal oxides, and carbon-based catalysts.^[4] Among them, metal and nitrogen-codoped carbon (M-N-C) systems have been considered as one of the most promising candidates in place of Pt-based electrocatalysts.^[5] Especially, Fe-N-C catalysts have gained a great attention due to their excellent ORR activity in both alkaline and acidic solutions.^[6] The Fe-N-C catalysts are generally obtained by pyrolysis of a compound of iron salts, nitrogen–carbon precursors at high temperature.^[7] However, such preparation methods often cause heterogeneous morphologies with unequal distribution of active centers toward ORR.^[8]

Recently, zeolitic imidazole frameworks (ZIFs), a subclass of metal-organic frameworks (MOFs) with versatile surface geometry, large surface area, abundant

pores, and N species, have been regarded as suitable precursors to fabricate structure-tailored carbon-based materials.^[9] A number of Fe-doped ZIF-derived carbon materials have been reported as effective ORR electrocatalysts.^[5,10] To prepare homogenous catalysts, Chen et al. demonstrated a cage-encapsulated strategy to construct Fe(acac)₃@ZIF-8 precursors for Fe-N-C catalysts.^[10a] And it has been reported that Fe²⁺ is preferred compared to Fe³⁺ to realize homogeneous Fe doping in ZIF-8 owing to the significant structural distortion with Fe³⁺ substitution for Zn²⁺.^[10b] Moreover, bimetallic active sites have been introduced by Wang et al. to further

Z. Wang, H. Jin, T. Meng, J. Yang, Prof. D. He, Prof. S. Mu
State Key Laboratory of Advanced Technology for Materials Synthesis and Processing
Wuhan University of Technology
Wuhan 430070, P. R. China
E-mail: hedaping@whut.edu.cn; msc@whut.edu.cn
K. Liao, W. Meng
Faculty of Materials Science and Chemistry
China University of Geosciences
Wuhan 430074, China

 The ORCID identification number(s) for the author(s) of this article can be found under <https://doi.org/10.1002/adfm.201802596>.

Prof. D. He
Hubei Engineering Research Center of RF-Microwave Technology and Application Wuhan
University of Technology
Wuhan 430070, China
Dr. Y. Xiong
Michael Grätzel Center for Mesoscopic Solar Cells (MGC)
Wuhan National Laboratory for Optoelectronics
School of Optical and Electronic Information
Huazhong University of Science and Technology
Wuhan 430074, China
E-mail: yuli.xiong@yahoo.com

DOI: 10.1002/adfm.201802596

enhance the ORR activity of Fe-N-C, who developed a catalyst with Fe-Co dual sites embedded in N-doped carbon, exhibiting excellent ORR activity and stability in acidic electrolytes.^[11]

Theoretical calculations have proposed that Cu possesses the uppermost activity for ORR among nonprecious transition metals because its position is close to Pt at the top of the “volcano plot.”^[12] However, Cu-based carbon materials obtained via pyrolysis tend to be plagued by self-aggregation, irreversible integration, and surface oxidation, owing to the large diffusion coefficient of Cu ions, which are unfavorable to their electrocatalytic performances.^[13] Recently, Cu-doped ZIF-8 has been studied.^[8,14] When the content of Cu ions in ZIF-8 matrix reaches a limit, they cannot be entirely stabilized by N-doped sites and partially reduced to metallic Cu atoms, and then aggregated into nanoparticles during pyrolysis.

In this work, the copper foil was employed to introduce Fe²⁺ and Cu²⁺ by a simple ionic reaction (2Fe³⁺ + Cu = Cu²⁺ + 2Fe²⁺) and minimize the oxidation reaction of Fe²⁺ to Fe³⁺ species during the growth of ZIF-8. The synthesis process of Cu@Fe-N-C is represented schematically in Figure 1a. The resulting Cu@Fe-N-C had a morphology of truncated rhombic dodecahedron with uniform distribution of Fe and Cu species. Owing to its bimetallic active sites, large surface area, high nitrogen doping level, and conductive carbon frameworks, Cu@Fe-N-C exhibited excellent ORR performance, which outperformed most Pt-free catalysts and the commercial Pt/C in an alkaline medium. When in an acidic medium, its performances were also comparable to Pt/C. To expand this catalyst for practical applications, we further used Cu@Fe-N-C to construct primary zinc–air batteries, which showed a high peak power density of 92 mW cm⁻² and excellent stability.

2. Results and Discussion

2.1. Electrocatalyst Characterizations

The morphology of FeCu-ZIF and Cu@Fe-N-C was characterized by scanning electron microscopy (SEM) and transmission electron microscopy (TEM). As shown in Figure 1b, FeCu-ZIF had a morphology of truncated rhombic dodecahedron, which was different from ZIF-8, Cu-ZIF (rhombic dodecahedron), and Fe-ZIF (without dodecahedron morphology) (Figure S1, Supporting Information). Obviously, the introduction of Fe²⁺ and Cu²⁺ resulted in a morphological change and significant increase in crystal size, owing to partial deprotonation of 2-methylimidazole linkers and broader growth directions in the presence of Fe and Cu ions during the growth of ZIF-8.^[6a,15] Cu@Fe-N-C retained its initial truncated rhombic dodecahedron shape after thermal treatment (Figure 1c). TEM image exhibited that small nanoparticles were distributed on the carbon matrix of Cu@Fe-N-C (Figure 2a). High-resolution TEM (HRTEM) image further indicated that Cu nanoparticles were encapsulated in graphitic carbon shells (Cu@C), and the lattice spacings were determined to be 0.345 and 0.209 nm, corresponding to the (002) plane of graphitic carbon and the (111) plane of metal Cu nanoparticles (Figure 2b), respectively.^[14a] Elemental mapping showed that Fe, N, and C were distributed homogeneously throughout the entire architecture, while Cu was mainly distributed in the form of dispersed nanoparticles (Figure 2c).

X-ray diffraction (XRD) patterns of FeCu-ZIF (Figure 2d), Fe-ZIF, and Cu-ZIF (Figure S2, Supporting Information) matched the pattern of ZIF-8 well, indicating their high crystallinities and similar zeolite-type structures. Among them, Cu@Fe-N-C showed a typical broad shoulder peak within the range of 20°–30° (2 theta) similar to that of N-C, which was assigned to the (002) plane of the graphitic carbon. The other three peaks

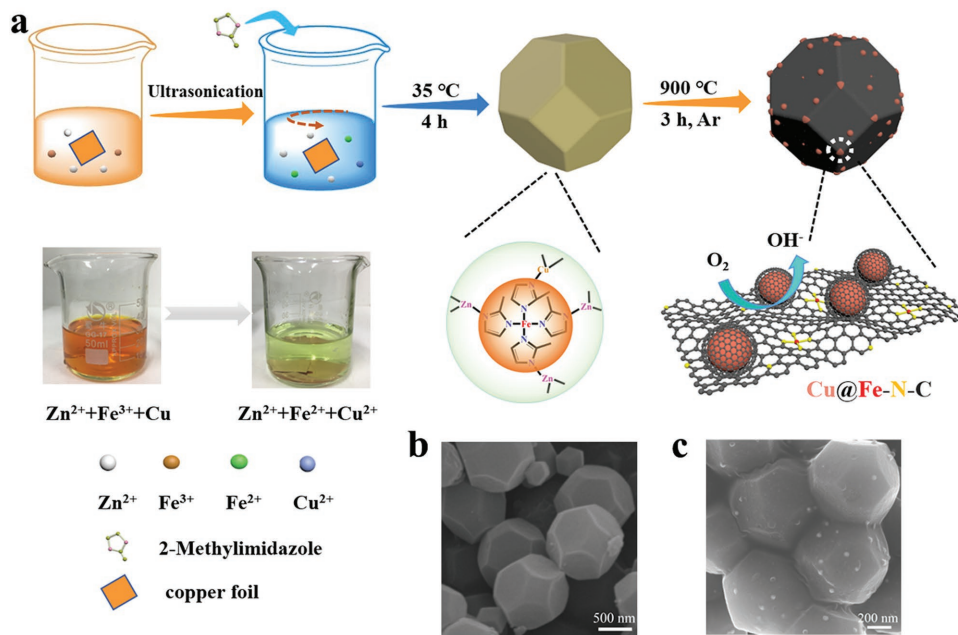


Figure 1. a) Schematic of the synthesis procedure of Cu@Fe-N-C. SEM images of b) FeCu-ZIF, and c) Cu@Fe-N-C.

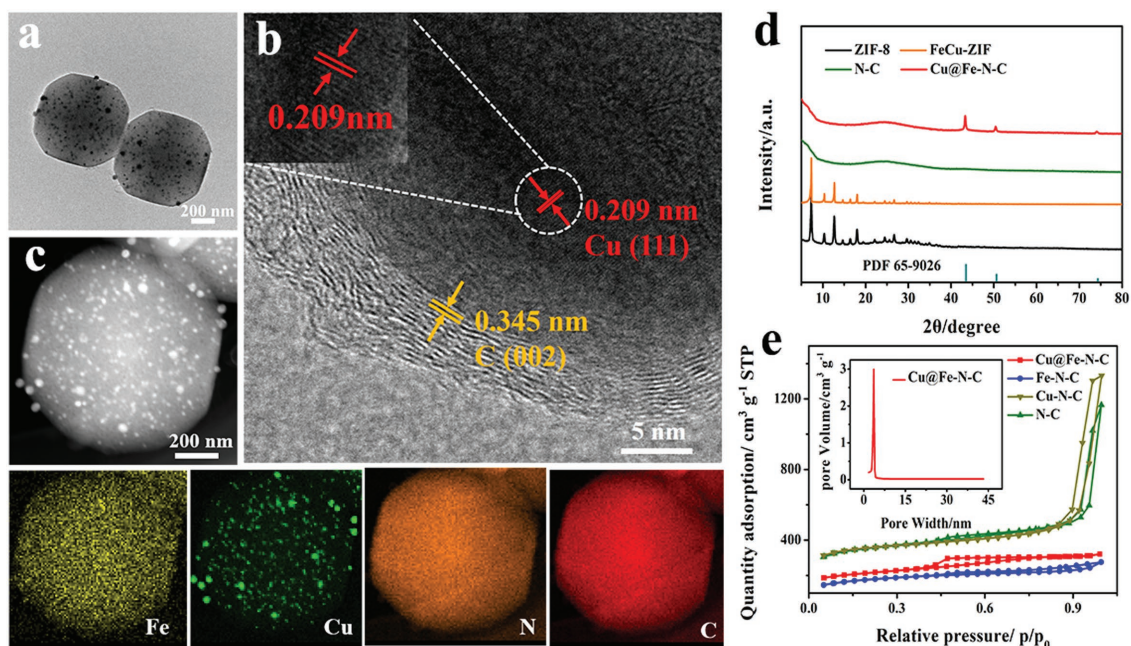


Figure 2. a) TEM and b) HRTEM images of Cu@Fe-N-C. c) TEM image and corresponding Fe, Cu, N, and C elemental mappings of Cu@Fe-N-C. d) XRD patterns of ZIF-8, FeCu-ZIF, N-C, and Cu@Fe-N-C. e) N_2 sorption isotherms of Cu@Fe-N-C, Fe-N-C, Cu-N-C, N-C and pore size distribution plots of Cu@Fe-N-C (inset).

belonged to metal Cu (PDF 65-9026), agreed with the results of the HRTEM. No peaks of iron species were observed, probably due to the low content (only 0.687 wt%) of iron, which was verified by inductively coupled plasma atomic emission spectroscopy (ICP-AES). As shown in Figure S2 (Supporting Information), the peaks of Fe-N-C corresponded to that of Fe_3O_4 (PDF 11-0614), possibly due to the partial oxidation of Fe^{2+} to Fe^{3+} .^[10b]

Raman spectra of Cu@Fe-N-C, Fe-N-C, Cu-N-C, and N-C exhibited two peaks at 1596 and 1332 cm^{-1} (Figure S3, Supporting Information), corresponding to the G band and D band, respectively, which indicated the existence of both defects and graphitization. The peak intensity ratio (I_D/I_G) of Cu@Fe-N-C was 1.05 but decreased to 1.01, 1.03, 0.99 for Fe-N-C, Cu-N-C, and N-C, respectively, demonstrating that Cu@Fe-N-C might possess more structural defects and a lower graphitization degree, beneficial to enhance the ORR activity.^[16]

To further obtain insight into the chemical composition in Cu@Fe-N-C and other samples, X-ray photoelectron spectroscopy (XPS) measurements were employed. The survey spectrum of Cu@Fe-N-C displayed distinctive peaks of Fe, Cu, N, O, and C, suggesting the existence of Fe and Cu in the Cu@Fe-N-C catalyst (Figure S4a, Supporting Information). Zn could be evaporated away at high temperatures over 800 °C because of the low boiling point Zn atoms (mp 420 °C, bp 907 °C). After the pyrolysis of FeCu-ZIF, the residual Zn (only 0.49 wt%) was found in Cu@Fe-N-C by ICP-AES and also confirmed by Zn 2p XPS spectrum (Figure S4b, Supporting Information). The high-resolution Fe 2p spectrum of Cu@Fe-N-C could be deconvoluted into five peaks at 710.7, 714.6, 719.2, 723.6, and 725.6 eV, which were attributed to the Fe(II) 2p_{3/2}, Fe(III) 2p_{3/2}, satellite, Fe(II) 2p_{1/2}, and Fe(III) 2p_{1/2} peak, respectively, suggesting that Fe existed as Fe(II) and Fe(III) in

the possible form of Fe-N_x.^[17] While the high-resolution Fe 2p spectrum of Fe-N-C signaled with three peaks at 708, 711, and 724 eV, assigned to Fe 2p_{3/2} and Fe 2p_{1/2} of Fe_3O_4 , and another peak at ≈ 708 eV attributed to metal Fe,^[18] corresponding to the results of XRD, and could be further verified by the magnetism identification (Figure S5, Supporting Information). As shown in Figure S6a (Supporting Information), the high-resolution Cu 2p_{3/2} spectrum showed two deconvoluted peaks at 932.7 and 934.9 eV, corresponding to Cu(0) and Cu(II)-O/N_x species, respectively. The coexistence of Cu nanoparticles and Cu-N bonds in Cu@Fe-N-C was confirmed by the XPS results, which was a typical catalytic site (N-Cu(II)-Cu⁰) reported by Xia and co-workers.^[14b] The high-resolution N 1s spectrum of Cu@Fe-N-C was deconvoluted into three peaks at 398.2, 399.5, 400.9 eV (Figure S6b, Supporting Information), assigned to pyridinic N, pyrrolic N, and graphitic N, respectively.^[19] Compared with Fe-N-C (3.28 at%), Cu-N-C (5.74 at%), and N-C (7.86 at%), Cu@Fe-N-C contained much higher N content (9.86 at%) (Figure S7, Supporting Information), indicating an enhanced N doping efficiency for Cu@Fe-N-C. Furthermore, the content of pyridinic N and graphitic N, as active sites for ORR, was 76% of the total N content in Cu@Fe-N-C.^[2]

The N_2 adsorption/desorption isotherm was carried out to characterize the surface area and porosity of Cu@Fe-N-C, Fe-N-C, Cu-N-C, and N-C. As shown in Figure 2e, samples Cu-N-C and N-C displayed Type I isotherms, while Cu@Fe-N-C and Fe-N-C showed Type IV isotherms with hysteresis loops at high pressure region, generally ascribed to the mesoporous structure.^[4c] Such mesoporous structure can be further verified by the pore size distribution plots (inset). The Cu@Fe-N-C sample showed a relatively intensive pore distribution with an average pore size of ≈ 4 nm (Figure S8, Supporting

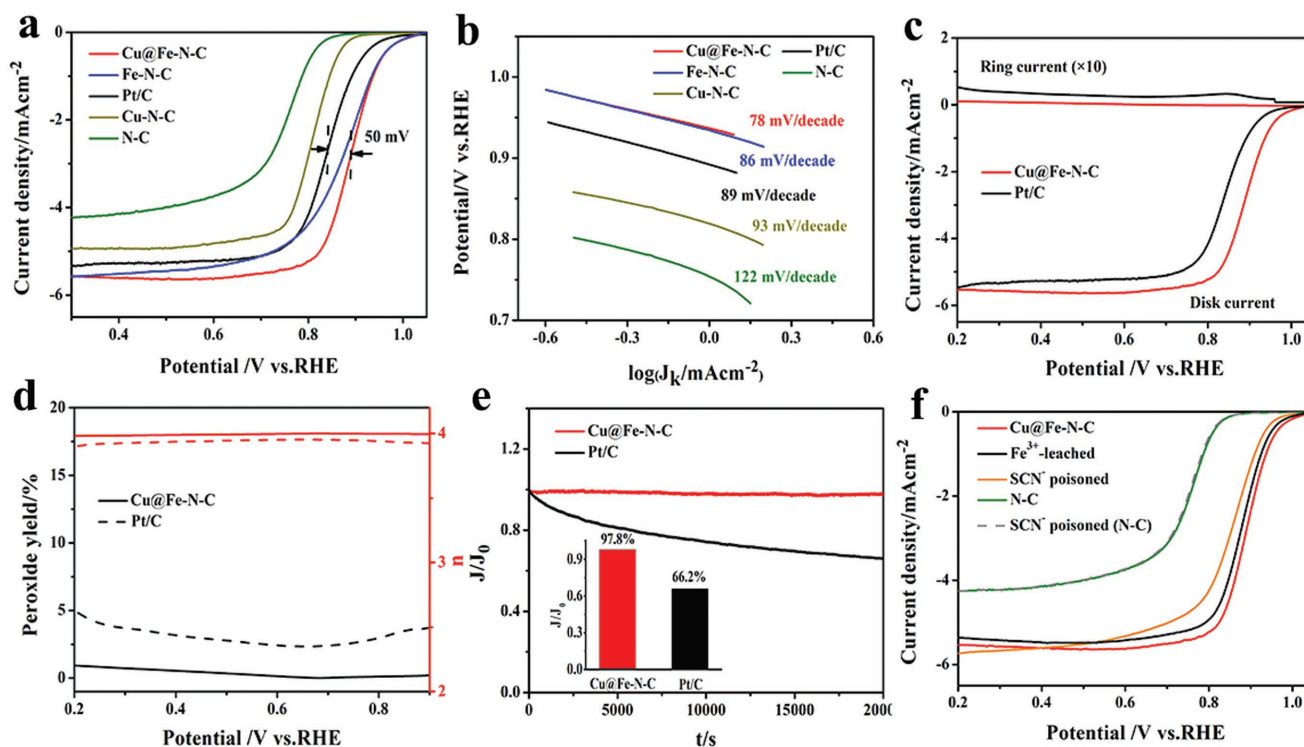


Figure 3. a) LSV curves of Cu@Fe-N-C, Fe-N-C, Pt/C, Cu-N-C, and N-C in O₂-saturated 0.1 M KOH solutions with a rotation speed of 1600 rpm and a sweep rate of 10 mV s⁻¹. b) Tafel slope values of Cu@Fe-N-C, Fe-N-C, Pt/C, Cu-N-C, and N-C. c) RRDE voltammograms and d) peroxide yield (black) as well as the calculated electron transfer number (*n*) (red) of Cu@Fe-N-C and Pt/C. e) The *i*-*t* chronoamperometric responses of Cu@Fe-N-C and Pt/C. f) Effect of Fe³⁺ leaching and SCN⁻ poisoning on the catalytic activity of Cu@Fe-N-C and N-C.

Information). The surface area of Cu@Fe-N-C was 726 m² g⁻¹, larger than that of Fe-N-C (608 m² g⁻¹), but smaller than that of Cu-N-C (1169 m² g⁻¹) and N-C (1204 m² g⁻¹), maybe due to the addition of Fe and Cu, resulting in significant increase in crystal size, as shown in SEM images.

2.2. Electrochemical Evaluation of Cu@Fe-N-C for ORR

To assess the ORR activity, the obtained catalysts were first evaluated in 0.1 M KOH. Cyclic voltammetry (CV) curves of Cu@Fe-N-C exhibited an increased cathodic peak at 0.845 V in an O₂-saturated electrolyte compared to that in an N₂-saturated electrolyte (Figure S9, Supporting Information), predicting its effective ORR electrocatalytic activity. After the high-temperature pyrolysis, because of the formation of bimetallic active sites and porous carbon frameworks, Cu@Fe-N-C exhibited excellent ORR performance, compared with FeCu-ZIF (Figure S10, Supporting Information). As shown in Figure 3a, linear sweep voltammetry (LSV) curves displayed that Cu@Fe-N-C possessed prominent electrocatalytic activity with much more positive onset-potential (*E*_{onset}) of 1.01 V, half-wave potential (*E*_{1/2}) of 0.892 V, and diffusion-limited current density of -5.52 mA cm⁻², which were better than those of commercial Pt/C (0.95 V, 0.842 V, -5.22 mA cm⁻², respectively) and most reported nonprecious ORR electrocatalysts (Table S1, Supporting Information). We also investigated the effects of different ratio of Zn/Fe/Cu on performance, which could be

simply tuned by changing the mass of Zn(NO₃)₂·6H₂O and Fe(NO₃)₃·9H₂O. As shown in Figure S11 (Supporting Information), the sample with the ratio 10:2:1 of Zn/Fe/Cu had the best ORR performance compared with other samples.

The Tafel slope of Cu@Fe-N-C was calculated to be 78 mV dec⁻¹, lower than that of Fe-N-C (86 mV dec⁻¹), Pt/C (89 mV dec⁻¹), Cu-N-C (93 mV dec⁻¹), and N-C (122 mV dec⁻¹), demonstrating that the Cu@Fe-N-C catalyst possessed more desirable ORR kinetics (Figure 3b). To gain further insight into the reaction mechanism of Cu@Fe-N-C, the rotating disk electrode (RDE) measurements were conducted at various rotation speeds from 400 to 1600 rpm, showing that the current densities were enhanced with the increasing rotation speed, while the onset potentials kept constant under different rotation speeds (Figure S12, Supporting Information). The inset of Figure S12 (Supporting Information) illustrated the Koutecky–Levich (K–L) plots of Cu@Fe-N-C, which displayed excellent linearity under different potentials, indicating that the transferred electron numbers per oxygen molecule in ORR were almost the same. The average electron transfer number of Cu@Fe-N-C (*n*) calculated from K–L plots was 4.0, suggesting a four-electron oxygen reduction process for ORR. Rotating ring disk electrode (RRDE) was conducted to further verify the excellent ORR performance of Cu@Fe-N-C (Figure 3c,d). The results indicated that the H₂O₂ yield of Cu@Fe-N-C remained below 1% and the average electron transfer number obtained from the RRDE tests was 3.99, corresponding with the result from K–L plots, which meant that Cu@Fe-N-C possessed high ORR catalytic efficiency.

Apart from catalytic activity, the durability test was studied by $i-t$ chronoamperometric response. As shown in Figure 3e, the relative current of Cu@Fe-N-C remained 97.8% after 20 000 s, much better than that of commercial Pt/C (66.2%). Meanwhile, LSV curves of Cu@Fe-N-C and Pt/C were conducted before and after $i-t$ curves. The half-wave potential of Cu@Fe-N-C decreased only 2 mV, but 29 mV loss of Pt/C after 20 000 s (Figure S13, Supporting Information), indicating that Cu@Fe-N-C had superb stability. In addition, methanol tolerance was measured by $i-t$ chronoamperometric response under the same condition with the addition of 1 M methanol. As shown in Figure S14 (Supporting Information), the current density of Pt/C dropped sharply, whereas it recovered rapidly after a transitory disturbance for Cu@Fe-N-C, indicating the superb methanol resistance ability.

It is well known that transition metals are very sensitive and reactive to SCN^- , which can poison metal-centered catalytic sites by coordinating with metallic species strongly in carbon-based materials.^[20] Therefore, to properly ascertain the influence of Fe and Cu species, Fe^{3+} leaching and SCN^- ions poisoning experiments were performed. The Cu particles were partially removed by dispersing the sample in 0.1 M $\text{Fe}(\text{NO}_3)_3$ aqueous solutions at ambient condition for 24 h. Even though Fe^{3+} leaching cannot completely remove Cu particles (Figure S15, Supporting Information), the changes on catalytic performance suggested that they could promote the ORR activity (Figure 3f). Removing the Cu nanoparticles might destroy N-Cu(II)-Cu⁰ sites, because the Cu(II) center coordinated with N sites was also stabilized by neighboring Cu nanoparticles.^[14] Moreover, The Cu@Fe-N-C

had a lower electrochemical reaction resistance compared to removing Cu nanoparticles as revealed by electrochemical impedance spectroscopy (EIS) measurements, suggesting the enhanced electron transport and fast kinetic process for Cu@Fe-N-C (Figure S16, Supporting Information). The ORR activity displayed a significant drop after adding 0.01 M KSCN, signifying a strong SCN^- ion coordination and blockage of the active Fe/Cu-N_x sites. To further confirm that Fe/Cu-N coupling centers and Cu@C were the main active sites, the metal-free N-doped carbon framework (N-C) was also analyzed under similar conditions. The ORR activity of N-C showed no significant degradation (Figure 3f), indicating a negligible effect of SCN^- ion attack on the nitrogen functionalities.

Furthermore, the ORR performance was also investigated in acidic media tested by both RDE and RRDE methods. A similar operation occurred in 0.5 M H_2SO_4 . Interestingly, Cu@Fe-N-C was also active and stable for ORR in acidic solution. As shown in Figure 4a, the E_{onset} and $E_{1/2}$ of Cu@Fe-N-C were 0.88 and 0.761 V, respectively, which were comparable to that of Pt/C and higher than most of other nonprecious metal-based catalysts (Table S2, Supporting Information). The Tafel slope of Cu@Fe-N-C (81 mV dec⁻¹) was smaller than that of Fe-N-C (94 mV dec⁻¹), Cu-N-C (235 mV dec⁻¹), and N-C (491 mV dec⁻¹), almost the same as Pt/C (65 mV dec⁻¹), which revealed a semblable kinetic process for Cu@Fe-N-C and Pt/C (Figure 4b). The electron transfer number of Cu@Fe-N-C calculated from K-L plots (Figure 4c) was 3.81. The H_2O_2 yield of Cu@Fe-N-C was below 4% in the tested potential range and the average electron transfer number obtained from the RRDE tests was 3.93,

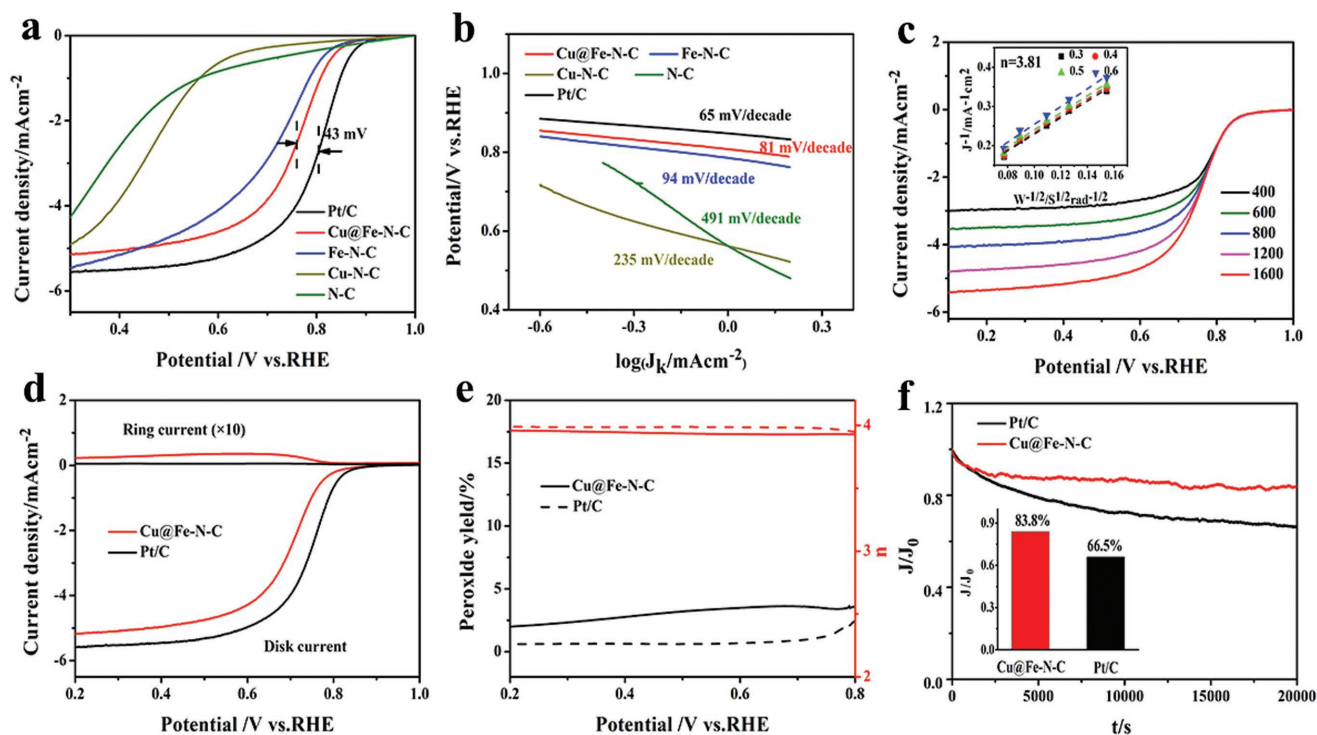


Figure 4. a) LSV curves of Cu@Fe-N-C, Fe-N-C, Pt/C, Cu-N-C, and N-C in O_2 -saturated 0.5 M H_2SO_4 solutions with a rotation speed of 1600 rpm and a sweep rate of 10 mV s^{-1} . b) Tafel slope values of Cu@Fe-N-C, Fe-N-C, Pt/C, Cu-N-C, and N-C. c) LSV curves of Cu@Fe-N-C at different rotation speeds and corresponding K-L plots (inset). d) RRDE voltammograms and e) peroxide yield (black) as well as the calculated electron transfer number (n) (red) of Cu@Fe-N-C and Pt/C. f) The $i-t$ chronoamperometric responses of Cu@Fe-N-C and Pt/C.

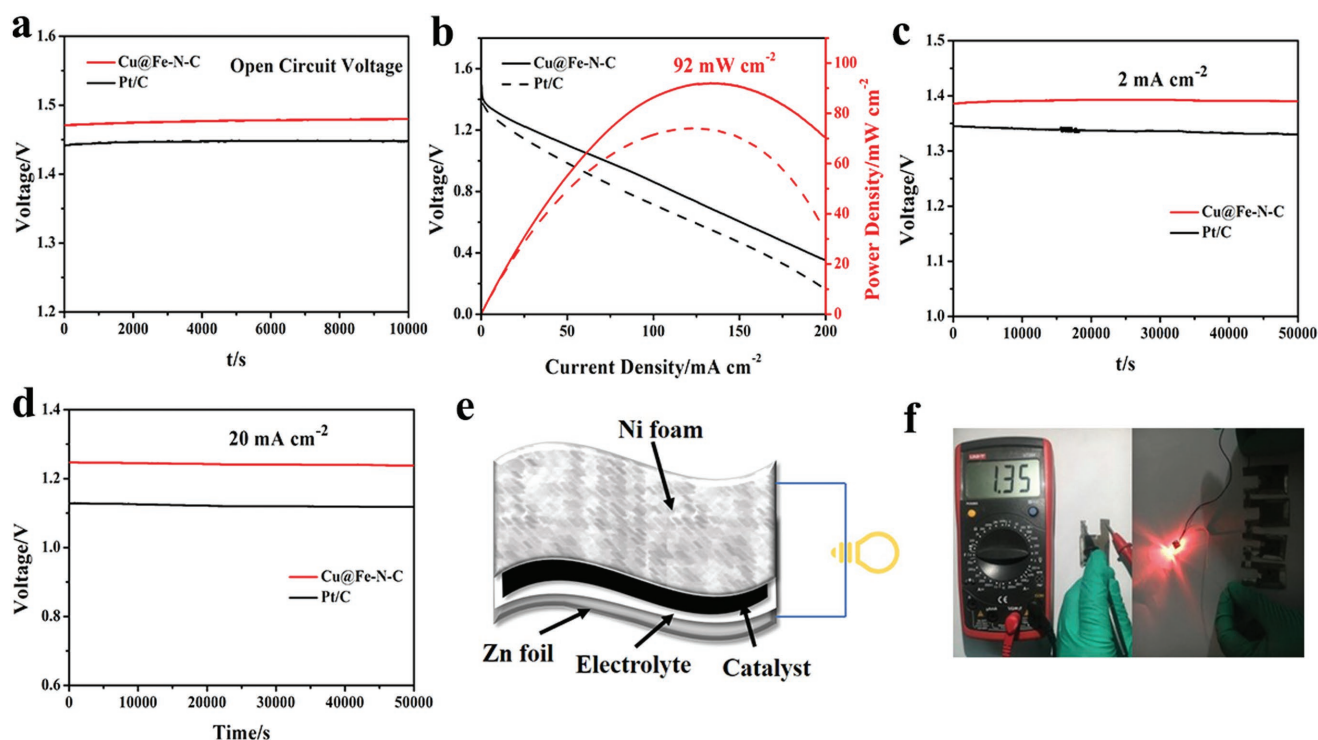


Figure 5. a) Open circuit voltage measurements of zinc–air batteries with Cu@Fe-N-C and Pt/C as the cathode catalysts. b) Polarization and power density curves of the zinc–air batteries with Cu@Fe-N-C and Pt/C as the cathode catalysts. Long-time galvanostatic discharge curves of zinc–air batteries with Cu@Fe-N-C and Pt/C as the cathode catalysts at c) 2 mA cm⁻² and d) 20 mA cm⁻². e) Schematic illustration of the all-solid-state zinc–air battery. f) Photograph of all-solid-state zinc–air battery displaying a measured open circuit voltage of 1.35 V and a lighted LED powered by four all-solid-state zinc–air batteries interconnected in series.

close to that of Pt/C (3.98) (Figure 4d,e). The $i-t$ curves were also used to study the durability and the methanol resistance of Cu@Fe-N-C and Pt/C in 0.5 M H₂SO₄. In consequence, the relative current of Cu@Fe-N-C remained 83.8% after 20 000 s of continuous operation, while only 66.5% was left for Pt/C (Figure 4f). Furthermore, the half-wave potential decline of Cu@Fe-N-C was 17 mV, much lower than that of Pt/C (58 mV) (Figure S17, Supporting Information). As shown in Figure S18 (Supporting Information), during the $i-t$ test, no obvious impact occurred on the current of Cu@Fe-N-C when 1 M methanol was injected into the system, while the current of Pt/C jumped instantaneously due to methanol oxidation reaction.

The outstanding electrocatalytic performances and stability of Cu@Fe-N-C have been demonstrated in our experimental results. We believe that its high activity is attributed to the following factors. The first one is the bimetallic active sites of Fe/Cu-N and Cu@C, which are regarded among the most efficient active sites for catalyzing ORR. Meanwhile, the introduction of Fe and Cu not only provided metal electrocatalytic site, but also enhanced N doping efficiency and a higher ratio of pyridinic, which are critical for electrocatalysis.^[21] The second factor is that the large surface area and mesoporous structure with abundant structural defects in the carbon matrix afforded more exposure of active sites as well as promoted the mass-transfer. Finally, the well-defined framework with Cu nanoparticles possessed high conductivity that enhanced efficient electron transport.

2.3. Zinc–Air Battery Performance

To this end, a home-made zinc–air battery was constructed using the Cu@Fe-N-C electrocatalyst dispersed on the hydrophobic carbon paper as the air cathode, 6 M KOH solution with 0.2 M zinc acetate as the electrolyte and zinc foil as the anode. Figure 5a shows that the Cu@Fe-N-C based zinc–air battery had an open-circuit voltage of 1.48 V, higher than Pt/C (1.45 V). The polarization and power density curves (Figure 5b) displayed that the zinc–air battery assembled from Cu@Fe-N-C owned a peak power density of 92 mW cm⁻², superior to that of Pt/C (74 mW cm⁻²) and most reported zinc–air batteries based on carbon-based nanomaterials (Table S3, Supporting Information). Our primary batteries were also durable. As shown in Figure 5c,d, when being galvanostatically discharged at a current density of 2 and 20 mA cm⁻² for 50 000 s, only a small activity loss was observed. To meet specific energy needs of practical applications, we further constructed a home-made all-solid-state battery according to Figure 5e; such a battery showed a high open-circuit voltage of 1.35 V, and only four batteries in series could effectively power a light emitting diode (Figure 5f).

3. Conclusion

In summary, an Fe, Cu-coordinated ZIF-derived carbon framework was facilely prepared and applied as highly active electrocatalyst for ORR. Attributed to bimetallic active sites,

high active N content and mesoporous architecture with large surface area of $726 \text{ m}^2 \text{ g}^{-1}$, the obtained Cu@Fe-N-C possessed a superior ORR performance with a half-wave potential of 0.892 V, excellent stability ($\approx 98\%$ activity retention after 20 000 s), and methanol resistance ability when compared with Pt/C in 0.1 M KOH. And, it also exhibits outstanding ORR activity and durability in an acidic medium. The primary zinc-air battery based on the Cu@Fe-N-C air-cathode demonstrated a high peak power density of 92 mW cm^{-2} as well as excellent durability. This work opens up a new opportunity for rational design and construction of high-performance nonprecious-metal catalysts for energy conversion and storage applications.

4. Experimental Section

Syntheses of ZIF-8: 2-methylimidazole (1314 mg) and $\text{Zn}(\text{NO}_3)_2 \cdot 6\text{H}_2\text{O}$ (594 mg) was dissolved in 30 mL methanol under ultrasound for 10 min to form a clear solution, respectively. Then, the first solution was added into the second solution under stirring, and the final mixture was stirred constantly at 35°C for 4 h to form ZIF-8. The obtained product was collected by centrifugation, followed by washing with methanol for three times and drying at 60°C under vacuum for overnight.

Syntheses of FeCu-ZIF: The synthesis procedure of FeCu-ZIF was similar to that of ZIF-8. First, the copper foil ($2 \times 2 \text{ cm}^2$) was cleaned and etched with 3 M HCl for 15 min to remove the surface oxide layer, and then rinsed with deionized water and methanol for three times in an ultrasound bath, respectively. Next, $\text{Zn}(\text{NO}_3)_2 \cdot 6\text{H}_2\text{O}$ (458 mg) and $\text{Fe}(\text{NO}_3)_3 \cdot 9\text{H}_2\text{O}$ (124 mg) were dissolved in 30 mL methanol, followed by ultrasound with three copper foil for 1 h to ensure there is no existence of Fe^{3+} . The rest synthesis process was the same as that of ZIF-8 mentioned above.

For comparison, Fe-ZIF, Cu-ZIF were synthesized following the same preparation procedures using $\text{Zn}(\text{NO}_3)_2 \cdot 6\text{H}_2\text{O}$ and $\text{FeSO}_4 \cdot 7\text{H}_2\text{O}$ or $\text{Cu}(\text{NO}_3)_2 \cdot 3\text{H}_2\text{O}$, respectively.

Syntheses of Cu@Fe-N-C: Cu@Fe-N-C was obtained by pyrolyzing under an Ar atmosphere in a tube furnace. The sample was calcined at 900°C with a rate of 5°C min^{-1} and maintained at 900°C for 3 h. Then it was naturally cooled to room temperature. Fe-N-C, Cu-N-C, and N-C were obtained by pyrolysis of Fe-ZIF, Cu-ZIF, and ZIF-8 at the same process.

Electrochemical Characterizations: The electrochemical measurements for ORR were carried out at room temperature on an Autolab PGSTAT302N electrochemical workstation with a standard three-electrode system. An RDE equipment was connected to the three-electrode system to characterize the ORR activity. A glassy carbon (GC) disk with diameter of 5 mm was used as working electrode. Ag/AgCl (in alkaline media) or calomel electrode (in acidic media) with saturated KCl and platinum wire were chosen to be the reference and counter electrode, respectively. In this work, catalyst inks were prepared as follows: 5 mg of catalyst was ultrasonically dispersed in 1.02 mL solution containing 900 μL of isopropyl alcohol, 100 μL of water, and 20 μL of Nafion ionomer solution (5 wt%). The well-dispersed catalyst ink was pipetted onto the GC disk electrode with a loading of 0.5 mg cm^{-2} for nonprecious catalysts and $20 \mu\text{g cm}^{-2}$ for Pt/C catalyst, as the working electrode. The electrolyte (0.1 M KOH solution or 0.5 M H_2SO_4) was purged with pure N_2 or O_2 for at least 30 min to obtain the N_2/O_2 saturated solution before the ORR tests.

The CV measurements were tested in N_2 and O_2 -saturated 0.1 M KOH and 0.5 M H_2SO_4 at a scan rate of 50 mV s^{-1} . RDE/RRDE tests were measured at varying rotating rates from 400 to 1600 rpm with a scan rate of 10 mV s^{-1} in O_2 -saturated 0.1 M KOH and 0.5 M H_2SO_4 . The stability tests were measured by current versus time ($i-t$) chronoamperometric response.

Zinc-Air Battery Tests: The measurements of zinc-air batteries were evaluated under ambient conditions. Briefly, a polished zinc foil and

6.0 M KOH solution containing 0.2 M zinc acetate were used as anode and electrolyte, respectively. The cathode was prepared by loading Cu@Fe-N-C or Pt/C catalysts on the $1 \times 2 \text{ cm}$ carbon paper (catalyst loading amount of 1.0 mg cm^{-2}). The all solid-state zinc-air battery was prepared by a clean zinc foil as anode and a solid polymer electrolyte as separator. The solid electrolyte was prepared as follow: 4.5 g polyvinyl alcohol powder was added into 45 mL solution of 6 M KOH with 0.2 M zinc acetate at 85°C to form a homogeneous viscous solution. Then, the solution was poured onto a glass disk and frozen for 12 h before use. To package the battery, a thin layer of the catalyst and zinc foil were placed on opposite sides of the polymer electrolyte film followed by placing nickel foam on the ambient dried catalyst layer as current collector. The components were firmly pressed together by roll-pressing and the catalyst loading was $\approx 1 \text{ mg cm}^{-2}$.

Supporting Information

Supporting Information is available from the Wiley Online Library or from the author.

Acknowledgements

This work was supported by the National Natural Science Foundation of China (51701146, 51672204), National Science Foundation for Post-doctoral Scientists of China (2016M602292), Special financial aid to post-doctor research fellow (2017T100548). The authors also acknowledge the Center for Materials Research and Analysis of Wuhan University of Technology for TEM (Prof. Xiaoqing Liu).

Conflict of Interest

The authors declare no conflict of interest.

Keywords

Fe-Cu coordination, oxygen reduction reaction, zinc-air batteries

Received: April 16, 2018

Revised: July 5, 2018

Published online: August 2, 2018

- [1] a) I. S. Amini, Z. Pu, X. Liu, K. A. Owusu, H. G. R. Monestel, F. O. Boakye, H. Zhang, S. Mu, *Adv. Funct. Mater.* **2017**, *27*, 1702300; b) H. Cheng, M.-L. Li, C.-Y. Su, N. Li, Z.-Q. Liu, *Adv. Funct. Mater.* **2017**, *27*, 1701833; c) T. Wang, Z. Kou, S. Mu, J. Liu, D. He, I. S. Amini, W. Meng, K. Zhou, Z. Luo, S. Chaemchuen, F. Verpoort, *Adv. Funct. Mater.* **2018**, *28*, 1705048.
- [2] J. Yang, H. Sun, H. Liang, H. Ji, L. Song, C. Gao, H. Xu, *Adv. Mater.* **2016**, *28*, 4606.
- [3] M. Shao, Q. Chang, J.-P. Dodelet, R. Chenitz, *Chem. Rev.* **2016**, *116*, 3594.
- [4] a) A. A. Gewirth, M. S. Thorum, *Inorg. Chem.* **2010**, *49*, 3557; b) L. Shang, H. Yu, X. Huang, T. Bian, R. Shi, Y. Zhao, G. I. Waterhouse, L. Z. Wu, C. H. Tung, T. Zhang, *Adv. Mater.* **2016**, *28*, 1668; c) N. Ramaswamy, U. Tylus, Q. Jia, S. Mukerjee, *J. Am. Chem. Soc.* **2013**, *135*, 15443.
- [5] T. Liu, P. Zhao, X. Hua, W. Luo, S. Chen, G. Cheng, *J. Mater. Chem. A* **2016**, *4*, 11357.

- [6] a) Y. Deng, Y. Dong, G. Wang, K. Sun, X. Shi, L. Zheng, X. Li, S. Liao, *ACS Appl. Mater. Interfaces* **2017**, 9, 9699; b) S. H. Ahn, X. Yu, A. Manthiram, *Adv. Mater.* **2017**, 29, 1606534; c) C.-Y. Su, H. Cheng, W. Li, Z.-Q. Liu, N. Li, Z. Hou, F.-Q. Bai, H.-X. Zhang, T.-Y. Ma, *Adv. Energy Mater.* **2017**, 7, 1602420.
- [7] a) G. Wu, K. L. More, C. M. Johnston, P. Zelenay, *Science* **2011**, 332, 443; b) A. Serov, K. Artyushkova, P. Atanassov, *Adv. Energy Mater.* **2014**, 4, 1301735.
- [8] H. Yu, A. Fisher, D. Cheng, D. Cao, *ACS Appl. Mater. Interfaces* **2016**, 8, 21431.
- [9] P. Su, H. Xiao, J. Zhao, Y. Yao, Z. Shao, C. Li, Q. Yang, *Chem. Sci.* **2013**, 4, 2941.
- [10] a) Y. Chen, S. Ji, Y. Wang, J. Dong, W. Chen, Z. Li, R. Shen, L. Zheng, Z. Zhuang, D. Wang, Y. Li, *Angew. Chem., Int. Ed.* **2017**, 56, 6937; b) X. Wang, H. Zhang, H. Lin, S. Gupta, C. Wang, Z. Tao, H. Fu, T. Wang, J. Zheng, G. Wu, X. Li, *Nano Energy* **2016**, 25, 110; c) D. He, Y. Xiong, J. Yang, X. Chen, Z. Deng, M. Pan, Y. Li, S. Mu, *J. Mater. Chem. A* **2017**, 5, 1930; d) H. Zhang, S. Hwang, M. Wang, Z. Feng, S. Karakalos, L. Luo, Z. Qiao, X. Xie, C. Wang, D. Su, Y. Shao, G. Wu, *J. Am. Chem. Soc.* **2017**, 139, 14143.
- [11] J. Wang, Z. Huang, W. Liu, C. Chang, H. Tang, Z. Li, W. Chen, C. Jia, T. Yao, S. Wei, Y. Wu, Y. Li, *J. Am. Chem. Soc.* **2017**, 139, 17281.
- [12] J. R. J. K. Nørskov, A. Logadottir, L. Lindqvist, *J. Phys. Chem. B* **2004**, 108, 17886.
- [13] M. Kuang, Q. Wang, P. Han, G. Zheng, *Adv. Energy Mater.* **2017**, 7, 1700193.
- [14] a) Q. Lai, J. Zhu, Y. Zhao, Y. Liang, J. He, J. Chen, *Small* **2017**, 13, 1700740; b) J. Wang, K. Wang, F. B. Wang, X. H. Xia, *Nat. Commun.* **2014**, 5, 5285.
- [15] a) A. Schejn, A. Aboulaich, L. Balan, V. Falk, J. Lalevée, G. Medjahdi, L. Aranda, K. Mozet, R. Schneider, *Catal. Sci. Technol.* **2015**, 5, 1829; b) M. He, J. Yao, Q. Liu, K. Wang, F. Chen, H. Wang, *Microporous Mesoporous Mater.* **2014**, 184, 55.
- [16] J. Zhu, H. Zhou, C. Zhang, J. Zhang, S. Mu, *Nanoscale* **2017**, 9, 13257.
- [17] N. R. Sahaie, U. I. Kramm, J. Steinberg, Y. Zhang, A. Thomas, T. Reier, J. P. Paraknowitsch, P. Strasser, *Nat. Commun.* **2015**, 6, 8618.
- [18] Z. S. Wu, S. Yang, Y. Sun, K. Parvez, X. Feng, K. Mullen, *J. Am. Chem. Soc.* **2012**, 134, 9082.
- [19] M. Wang, Y. Yang, X. Liu, Z. Pu, Z. Kou, P. Zhu, S. Mu, *Nanoscale* **2017**, 9, 7641.
- [20] I. S. Amiin, X. Liu, Z. Pu, W. Li, Q. Li, J. Zhang, H. Tang, H. Zhang, S. Mu, *Adv. Funct. Mater.* **2018**, 28, 1704638.
- [21] a) J. Liu, X. Sun, P. Song, Y. Zhang, W. Xing, W. Xu, *Adv. Mater.* **2013**, 25, 6879; b) W. Xia, J. Masa, M. Bron, W. Schuhmann, M. Muhler, *Electrochem. Commun.* **2011**, 13, 593.